RoS: Passive Smart Surface for Roadside-to-Vehicle Communication

John Nolan, Kun Qian, Xinyu Zhang*
University of California San Diego

ABSTRACT

Modern autonomous vehicles are commonly instrumented with radars for all-weather perception. Yet the radar functionality is limited to identifying the positions of reflectors in the environment. In this paper, we investigate the feasibility of smartening transportation infrastructure for the purpose of conveying richer information to automotive radars. We propose RoS, a passive PCB-fabricated surface which can be mechanically reconfigured to embed digital bits, and inform the radar much like visual road signs do to cameras. We design the RoS signage to act as a retrodirective reflector which can reflect signals back to the radar from wide viewing angles. We further introduce a spatial encoding scheme, which piggybacks information in the reflected analog signals based on the geometrical layout of the retroreflective elements. Our prototype fabrication and experimentation verifies the effectiveness of RoS as an RF "barcode" which is readable by radar in practical transportation environment.

CCS CONCEPTS

• **Hardware → Sensor applications and deployments**; **Printed circuit boards**.

KEYWORDS

Smart Surface, Intelligent Reflecting Surface, V2X, Millimeter Wave Radar, Van Atta Array

1 INTRODUCTION

If intelligent transportation systems (ITS) are to become a reality, reliable and abundant information about the environment will be crucial for an efficient and safe driving experience. Mainstream ITS technologies rely heavily on intelligent autonomous vehicles [2], with myriads of on-board sensors and rapidly evolving algorithms to approximate or even surpass human perception. Equally important however, is an increasingly intelligent civil infrastructure. A smart infrastructure that embeds cameras, sensors, and communication technologies can dramatically lower the perception
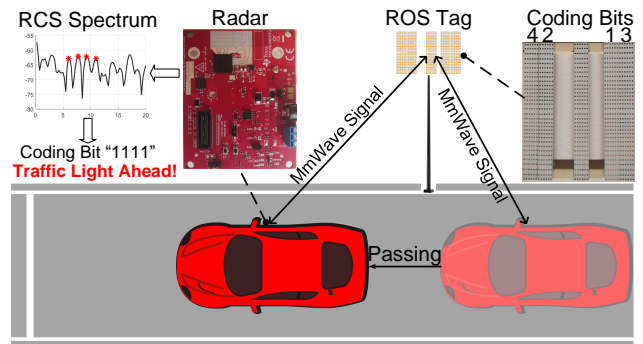
*John Nolan and Kun Qian are co-primary authors.

Figure 1: General working scenario of RoS.

requirements of the vehicles, accelerating the progress towards ITS.

One of the most crucial elements in transportation infrastructure is the road sign which displays traffic/speed/location information to oncoming vehicles. Substantial research has been devoted to automating the recognition of road signs through on-board cameras and computer vision algorithms [25]. However, cameras are fundamentally challenged by low-angle sunlight and poor visibility in adverse weather conditions (*e.g.*, fog, snow, and rain). Such limitations can be avoided by smartening road signs and embodying infrastructure-to-vehicle (I2V) communication technologies, such as RFID, DSRC, and C-V2X [47]. These solutions however, require heavily instrumented road signs and compatible vehicles which entail high deployment costs. In contrast, automotive radar have already been widely installed on modern vehicles to sense surrounding objects. If existing automotive radar could read road signs directly, deployment costs could be reduced significantly.

In this paper, we propose retroreflective radar readable road sign (RoS), a fully passive and chipless RF tag which overcomes the fundamental limitations of legacy visual signage with minimal deployment costs. Fig. 1 shows RoS and its general working scenario. A RoS tag consists of a collection of millimeter-wave (mmWave) antenna arrays which are designed on thin laminate boards and can be fabricated via common PCB manufacturing processes. The antenna arrays form a specially designed geometrical layout to create distinct reflection patterns that can be sensed by an automotive radar. The RoS tag's layout is mechanically reconfigurable, as the number and locations of the antenna arrays can be manually modified to create different reflection patterns. The tag can be erected preceding a legacy road sign as a complementary radar-readable sign. A vehicle *passing by* the tag can localize it, measure its reflection pattern, and decode the embedded information with its on-board radar. The vehicle can then notify the driver or take actions accordingly.

Detecting and decoding RoS in a dynamic automotive scenario poses many unique challenges. First of all, for RoS to work properly

and effectively with automotive radars, the RoS tag must be easily detectable in spite of the vehicle's varying viewing angles and distances. To increase the azimuth field-of-view (FoV), we use Van Atta arrays (VAAs) [49] as a fundamental building block for the tag. The VAAs retroreflect mmWave signals in the azimuth plane, *i.e.*, radar signals that impinge on the VAAs will be reflected back to the emitter. With VAAs, the RoS tag can create a quasi-omnidirectional reflection pattern and hence an electrically wide angular view. To increase the reading distance, RoS stacks multiple VAAs vertically to increase its overall reflectivity. The stacking of VAAs unfortunately, creates an unwanted beamforming effect where the beamwidth along the vertical dimension can become extremely narrow. Consequently, minor height misalignment between the radar and the tag may result in extremely weak reflections and hence, decoding failure. To mitigate the impact of such misalignment, we introduce an *elevation beam shaping* mechanism which can synthesize wider elevation beams without impacting the retroreflectivity on the azimuth plane. The beam shaping is achieved by treating the VAAs within a stack as individual antenna "elements", and applying a set of pre-determined phase weights on them. The phase weighting is in term created by optimizing the relative lengths and layouts of the transmission lines (TLs) within each VAA.

The second design challenge lies in interference due to background reflections. In the automotive environment, a plethora of other objects, *e.g.*, pedestrians and street lamps, can easily overwhelm the return signal from an RoS tag due to their large size and strong reflectivity. To filter out such background interference, we design a *polarization switching VAA (PSVAA)* for the tag, which alters the polarization of the incident signals to an orthogonal polarity while reflections from ordinary roadside objects remain intact. With this measure, the radar can easily single out the tag's reflections and suppress the environmental impact.

Third, it is non-trivial to encode information in a deterministic way using a passive mmWave tag alone. A straightforward encoding method is to print random metallic geometries on the tag, which can be mapped to certain radiation patterns using a machine learning model [28]. However, this method loses the retroreflective property and its non-explainable models have no performance guarantees. In other words, it is unclear how reliably the different symbols can be discriminated by the radar and how many bits of information it can actually encode. In RoS, we overcome such limitations through a novel *spatial coding* scheme. We build a deterministic model which establishes the relationship between the *geometrical layout* of multiple PSVAAs and the corresponding *reflection pattern*. In this way, the RoS tag can encode information by simply positioning the VAAs following our model, and the radar can decode data bits by sampling the reflection signal strengths across multiple locations.

Finally, it is challenging to accurately measure the *reflection pattern* of a tag in the automotive scenario with a moving radar. To overcome this challenge, RoS leverages the self-tracking capabilities of modern vehicles to obtain a coarse estimation of the relative tag-radar position. It further uses two features, *i.e.*, point cloud size and reflection loss, to discriminate the tag from other objects. The radar can then beamform its signals to consistently "spotlight" on the tag.

We have fabricated RoS tags and conducted extensive field experiments with TI's experimental mmWave radar [22]. Although the radar has a relatively low transmit power and low sensitivity, the decoding SNR of RoS consistently exceeds 14 dB in typical scenarios, which translates into a bit error rate below 0.6%. The RoS tag can be reliably decoded by the radar at a distance of up to 6 m, which fits common transportation scenarios where a vehicle passes by the tag along a multi-lane road.

In summary, the main contributions of RoS include:

(i) Fully passive retroreflective smart surface comprised of an array of VAAs. We have designed a passive chipless tag that is retroreflective for 77-81 GHz automotive radar signals. Owing to the novel polarization switching and elevation beam shaping mechanisms, our RoS tag can be reliably detected by a radar in practical roadway conditions.

(ii) Spatial coding scheme. We design a novel spatial coding scheme that exploits the deterministic relation between the tag's geometrical layout and its reflection pattern. We further introduce mechanisms to enable the radar to accurately measure the tag's reflection pattern in a dynamic automotive environment.

(iii) Implementation and experimental validation. We have implemented RoS using the standard PCB fabrication process which allows for mass production and reconfiguration of the signage. Our experiments verify the feasibility and accuracy of RoS, and its usefulness as a new component in ITS.

2 RELATED WORK

Wireless I2V communications. A rich literature exists on wireless communications between infrastructure and vehicles (I2V) which primarily focuses on improving efficiency and reliability. DSRC and cellular C-V2X represent two mainstream I2V technologies. Both are witnessing limited deployment due to the cost in instrumenting the vehicles and upgrading the base stations. Electronic toll collection systems (E-ZPass) have been deployed on many roadway intersections and traffic hubs. E-ZPass consists of a reader embedded within transportation infrastructure that queries a battery-powered RFID tag mounted on a vehicle. Recent work adapts RFID localization technologies to position vehicles with E-ZPass onboard [1]. RoS differs from conventional I2V in that the roadside infrastructure is fully passive and does not require dedicated radio hardware. The main downside of RoS however, lies in that it only encodes a fixed amount of information similar to conventional road signs.

Vision based technologies for road-to-vehicle communication. Our work is motivated by the growing interest in ITS which automates roadway infrastructure and vehicles to improve efficiency and safety. Market solutions for such services already exist, including smart streetlights for parking spot checking [8], smart intersections that can monitor vehicle density and control traffic lights [10], *etc.* These solutions require a smart camera to capture and process roadway status information. On-board computer vision technologies have also been widely explored to assist drivers by reducing missed road-signs and ultimately reduce accidents [25]. These technologies however, are plagued by variable lighting conditions, sign orientation, sign aging, shadows of near-by objects, and adverse weather conditions [7, 14].

To improve visibility, road signs today typically use a retroreflective coating and some even install LED lights. LEDs can be

further renovated to modulate information which can be captured and decoded by on-vehicle cameras [23]. RetroI2V [59] exploits visible light backscatter communication in the form of an active road sign that can modulate the polarization of the vehicle's LED headlight and reflect the modulated signals to convey information. Such systems still entail heavy instrumentation of both infrastructure and vehicles. In addition, they bear many of the same intrinsic limitations as camera vision, *i.e.*, vulnerability to adverse weather conditions, although their detection range may be longer due to the use of high dynamic range photodiode sensors.

Chip and chipless RFID. RFID technologies have proliferated research areas such as wireless communications, energy harvesting, object tracking, human-object interaction, *etc.* [16, 30, 39, 48, 58]. An RFID system comprises of an interrogating reader and a tag with a RFID chip that is responsible for storing data and backscattering signals. In [17, 32, 37], RFID tags are used to inventory road signs and land marks. Vehicles with RFID readers can detect these tags and decode information of road signs. Although RFID tags are low cost and have high data encoding capabilities, it requires vehicles to mount expensive RFID readers. In contrast, mmWave radars are already abundant on vehicles today and are envisioned to be reused with mmWave tags at low cost. In addition, due to large antenna sizes in UHF band, it is difficult to realize retro-directive RFID tags. Consequently, interference will become a daunting challenge in areas with densely populated vehicles and tags. Ultra-low power designs using power harvesters [38, 50] can be used to design passive RFID tags that modulate the backscattered mmWave signal. However, with a required input power about 2 dBm, these ultra-low power designs would have severely limited communication range at mmWave band.

Chipless RFID can be considered as an RF barcode, manufactured through PCB printing or even inkjet printing [21] which eliminates the IC cost. Chipless RFID tags can encode information in the frequency or time domain. A common frequency domain technique is to use notch filters that attenuate specific frequency bins to create unique identification signatures [5, 16, 24, 40]. Time domain encoding generally inscribes information by modulating the timing of pulses reflected back to the interrogator. Some examples include surface-acoustic-wave (SAW) tags [41] or delay lines [51]. Despite the low-cost, chipless tags have a major drawback–they generally operate in smaller interrogation zones and have limited information encoding capabilities compared to the IC tag variants. RoS aims to bring the benefits of fully passive, chipless RFID tags into the automotive sensing domain. To this end, RoS renovates the tag design in two unique ways: *(i)* It leverages an array of retro-directive VAAs to improve the reliability, reading range, and angular field-of-view. *(ii)* It utilizes a scalable spatial domain encoding mechanism to embed information in the RCS of the tag. Besides, RoS enables a radar to interrogate the tag in practical driving scenarios.

Retro-directive antennas. Retro-directive antennas automatically redirect incoming signals back to the direction of the source. The most widely known retro-directive antenna is the corner-reflector [27]. An alternative is active phase conjugation using a mixer or passive phase conjugation through VAAs. Since its invention in the 1960's [49], VAAs have been researched extensively to realize retroreflection. Many VAA designs have been implemented in the microwave frequency band [44, 63] using a variety of antenna

structures such as slots [33], rings [45] or patch [3].

The electromagnetic research literature has explored ways of combining retro-directive antenna designs with information encoding capabilities [27, 62]. In [62], information is stored in the frequency domain through the use of surface notch filters to attenuate specific frequencies creating a spectrum signature. In [53], the reflected signal phase is modulated by varying transmission line lengths or by frequency shifting the incident signal as in [26]. MmWave frequencies create new challenges for passive retro-directors. Notch filter becomes impractical because of the difficulty in achieving large filter gain at high frequency bands [13], whereas phase based methods become extremely sensitive to multipath.

In addition, many chipless backscatters have been developed using RF switch modulation [20, 29, 31, 52]. In Millimetro [52], long-range and identifiable tags at 24 GHz are designed using VAAs and RF switches. At design frequencies such as 900 MHz and 24 GHz, reasonable RCS values can be achieved with minimal effort. However, translating these designs to the 77 GHz automotive radar band (*i.e.*, 76-81 GHz) poses many challenges such as routing of the RF switches and obtaining sufficiently high RCS levels. For example, in REITS [29], a total of 10 elements are used to create a VAA with 5 pairs of antennas at 24 GHz. Moving to 77 GHz, this design would suffer an RCS reduction of 25.85 dB. To overcome this issue, many more antennas would be required, complicating the joint routing of transmission lines and RF switches.

In contrast, RoS represents the first work to create an array of retro-directive VAAs and use their spacial layout to encode data. The RoS tag does not require discrete RF components and is designed to be directly detectable and decodable by an automotive radar.

3 PRELIMINARY

3.1 Electromagnetic Signature of Objects

Radar signal propagation follows the well known round-trip path loss model [35]:

$$P_r = \frac{P_t G_t G_r \lambda^2 \sigma}{(4\pi)^3 d^4} \tag{1}$$

where P_r, P_t, G_t, G_r, λ, d and σ are the received signal strength (RSS), transmit (Tx) signal power, Tx gain, receive (Rx) gain, signal wavelength in freespace, radar-to-object distance, and the Radar Cross Section (*RCS*) of the object, respectively. This equation applies to a typical monostatic radar, *i.e.*, the Tx and Rx antennas are co-located.

The RSS level P_r is directly proportional to wavelength λ, posing a challenge at mmWave frequencies which suffer from higher attenuation loss compared to microwave signals. Practical mmWave radars often adopt MIMO beamforming, using multiple Tx/Rx antennas to increase the Tx/Rx gain to compensate for the larger attenuation.

The RCS σ is a measure of an object's detectability to a radar or how electrically large the object appears. Intuitively, RCS is the ratio between the backscatter power per steradian in the direction of the radar and the power density that is intercepted by the object. The RCS area of an object does not necessarily overlap with the physical cross-sectional area of that object. Instead, it depends upon other factors such as material reflectivity, incident polarization, the radar's viewing angles, and the directivity of the reflected
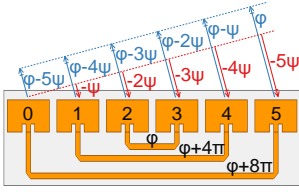
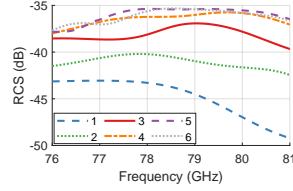**Figure 2: Retroreflective Van Atta array (VAA).**

Figure 3: RCS with different number of antenna pairs.

signals caused by the object's geometric shape. *The RoS tag is essentially a smart surface whose RCS can be configured to convey bits of information to the radar.*

3.2 Object Detection with FMCW Radar

Commercial mmWave radars typically transmit periodic frequency modulated continuous wave (FMCW) signals [46] whose frequency increases linearly within each frame period. The radar can localize an object by estimating the distance and angle of arrival (AoA) of reflected signals [57]. Distance estimation relies on counting the time-of-flight, whereas AoA estimation relies on an array of Rx antennas. For an object whose distance is d_o and AoA is θ_o, the baseband signal of the k-th Rx antenna is [46]:

$$s(t, k) = P_r e^{-4\pi i \frac{\gamma d_o}{c} t} e^{-2\pi i \frac{k \delta_a \cos \theta_o}{\lambda}}, \qquad (2)$$

where γ and c denote the FMCW frequency slope and light speed. δ_a represents the spacing between adjacent Rx antenna elements. The first phase term is due to the propagation delay between the radar and the object, while the second is due to the relative propagation delay between the Rx antennas.

To estimate the distance of the object, an IFFT is applied over the time domain t:

$$S_1(d, k) = \text{IFFT}[s(t, k)] \approx P_r \delta(d - d_o) e^{-2\pi i \frac{k \delta_a \cos \theta_o}{\lambda}}, \qquad (3)$$

$S_1(d, k)$ achieves the maximum when $d = d_o$. To further estimate the AoA of the object, the pseudo spectrum $S_2(d_o, \theta)$ is calculated by applying beamforming weights $w_k = e^{2\pi i \frac{k \delta_a \cos \theta}{\lambda}}$ to the frequency samples $S_1(d_o, k)$:

$$S(d_o, \theta) = \sum_k w_k S(d_o, k) \approx P_r \delta(\theta - \theta_o). \qquad (4)$$

When $\theta = \theta_o$, the RSS P_r can be approximated with $S(d_o, \theta_o)$.

In practice, by recognizing peaks at different distances in $S_1(d, k)$ and different AoAs for each distance in $S_2(d_o, \theta)$, the locations and reflected RSS of all prominent reflecting points can be estimated, generating a *radar point cloud*.

The radar's distance (range) resolution Δ_d, and angle resolution Δ_θ, is inversely proportional to the sampling bandwidth B and number of antennas N_a, respectively. For example, the recently developed TI automotive radar [22] has $B = 4$ GHz and $N_a = 8$, translating to $\Delta_d = 3.75$ cm and $\Delta_\theta = 14.3°$, respectively. It might be tempting to create a simple RF barcode by placing multiple metal pieces at predefined spots on a road sign to encode information, much like [28]. Unfortunately, given the coarse angle resolution, it is infeasible for a radar to discriminate the pieces at a few meters away. The specular reflection will also render such a barcode undetectable

unless the radar stays at its normal direction.

4 MMWAVE RETROREFLECTIVE TAG DESIGN

An RoS road sign must be easily detectable by a radar within a wide *angular range*, and be *distinguishable* from other irrelevant objects on the road. In addition, its RCS should be large enough, so that the reflected signals can be detected by a passing-by radar, which can be a few lanes away from the curb. RoS innovates an array of passive retroreflectors to meet these challenges, which will be detailed in this section.

4.1 Retroreflection within the Azimuth Plane

A primer on Van Atta Array (VAA). RoS realizes the mmWave retroreflector by extending the classical Van Atta Array (VAA) structure which was invented in the 1960's [49]. As shown in Fig. 2, a basic VAA consists of a linear array of antenna elements with equal spacing of $\frac{\lambda}{2}$. The symmetric elements (with respect to the center of the array) are interconnected by transmission lines (TLs). Signals received by each antenna are propagated through the TLs and re-radiated by its connected peer on the other end. Suppose an incident *far field* wavefront induces a phase offset, ψ, between adjacent antennas. The *incident signal phase* at the k-th antenna, relative to that at the 0-th antenna, is $-k\psi$. By setting the lengths of each TL to differ by multiples of λ_g (i.e., the wavelength of the signal guided in TLs), a constant wrapped phase offset φ is introduced for all signals propagating through the TLs. Consequently, given the number of antennas N, the k-th antenna receives and re-rediates the signal from the $(N-1-k)$-th antenna, whose phase is $\varphi - (N-1-k)\psi$. Its phase relative to the 0-th antenna is $(\varphi - (N - 1 - k)\psi) - (\varphi - (N - 1)\psi) = k\psi$, which is reversed compared to the phase of the incident signal arriving at it. In other words, *the re-radiated signal is steered back to the direction of arrival, i.e., the VAA is retroreflective.*

VAA design choices for RoS. The use of multiple incident and re-radiation antennas essentially makes the VAA a passive beamforming reflector which focuses towards the interrogator. Ideally, the more antenna pairs in a VAA, the larger its RCS should be. However, the aforementioned VAA model assumes a single tone signal whose guided wavelength is λ_g, whereas in RoS, the interrogator is a radar with a wide bandwidth, and hence the difference of the guided wavelength across frequencies becomes non-negligible. Furthermore, more antenna pairs means a longer TL length and more propagation loss which limits the RCS contribution of the outer antenna pairs. Thus, we analyze how to optimize the VAA design in RoS to account for these factors.

Recall that the different TLs differ by multiples of λ_g. The radar signals at different frequencies experience phase misalignment when propagating through variable length TLs. Consequently, the phase misalignment becomes unavoidable as the length difference between TLs increases. Suppose the bandwidth and center frequency of the radar are B and f_c, and the maximum length difference between the shortest and longest TL is δ_l, the maximum phase misalignment between the frequencies $f_c + \frac{B}{2}$ and $f_c - \frac{B}{2}$, is $2\pi \frac{B}{c_g} \delta_l$, where c_g is the signal propagation speed in the TLs. To avoid destructive interference between antenna pairs, the maximum phase misalignment should be smaller than $\frac{\pi}{2}$, i.e., $2\pi \frac{B}{c_g} \delta_l \leq \frac{\pi}{2}$.
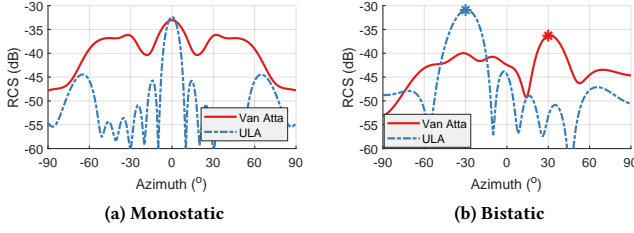
(a) Monostatic

(b) Bistatic

Figure 4: Comparison of the RCS of Van Atta Array (VAA) and Uniform Linear Array (ULA).

(a) Tx/Rx with orthogonal polarization
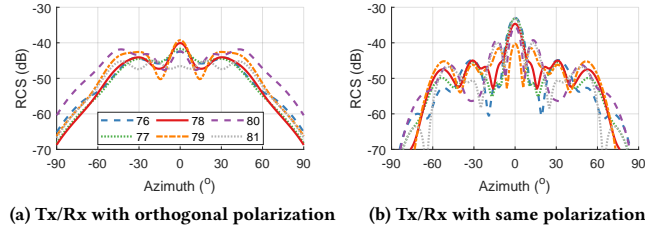
(b) Tx/Rx with same polarization

Figure 6: RCS of PSVAA across the 76-81 GHz frequency band.

For a typical automotive radar with $B = 4$ GHz, we have $\delta_l \leq 4.94\lambda_g$. Given that the total spacing between adjacent antenna pairs is $2 \cdot \frac{\lambda}{2} = \lambda$, the length difference of adjacent TLs, denoted as ΔL, should be at least λ to avoid antenna overlap. Accordingly, since ΔL must be an integer multiple of λ_g and $\lambda_g < \lambda$, the minimum ΔL needs to be $2\lambda_g$. Therefore, for RoS to retro-reflect automotive radar signals, *the optimal number of antenna pairs on each VAA is* $\lceil \frac{4.94\lambda_g}{2\lambda_g} \rceil = 3$.

Verifying the design choices. To verify the above design choices, we conduct experiments in Ansys HFSS, a 3D electromagnetic (EM) field simulator. We lay out VAAs with different number of antenna pairs and simulate their RCS across the wide frequency band of an automotive radar, *i.e.*, 76-81 GHz. As shown in Fig. 3, the RCS contribution per antenna pair is maximized with 3 antenna pairs and marginally increases beyond that which matches the above model. Thus, to maximize the utility in terms of RCS per antenna pair, *a VAA in RoS should have at most 3 antenna pairs.*

The ideal VAA model [49] assumes perfect lossless, point-scatter antennas and a single frequency. To verify the retroreflectivity of the VAA in the presence of practical wideband mmWave radar signals, we conduct another HFSS simulation and compare the 6-element VAA with a uniform linear array (ULA) of 6 patch antenna elements. The ULA can be considered as an ordinary reflective object comprised of a few metal patches. Fig. 4a shows the measured RCS when a monostatic radar passes by from different azimuth angles. We see that the VAA has a relatively flat RCS within a field-of-view (FoV) of approximately 120°, which verifies its retro-directive property. In contrast, the ULA acts like a specular reflector, and only responds with a strong RCS when the radar faces it straight on. Note that the FoV of the VAA or ULA cannot reach 180° since each patch antenna element itself has a limited radiation angle.

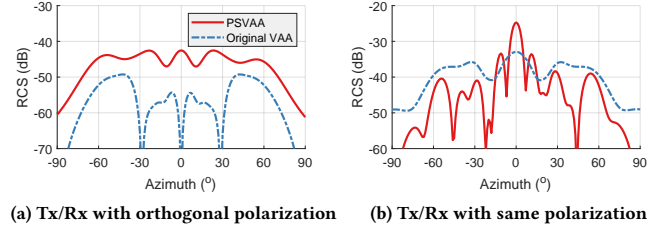A side benefit of retroreflectivity is that *interrogating radar signals*

(a) Tx/Rx with orthogonal polarization

(b) Tx/Rx with same polarization

Figure 5: Comparison between the RCS of PSVAA and original VAA.

arriving from different angles do not interfere with each other. Fig. 4b showcases a scenario where a radar interrogates the VAA at an angle of 30°, while the RCS is measured at different azimuth angles. We see that the ULA reflects the signals towards the symmetric direction (−30°), whereas the VAA redirects the signal back to the incoming angle. Although the VAA is imperfect and there exists leakage at other angles, the leaked signals are much weaker (5-13 dB lower), demonstrating that the interference of the VAA to directions other than the incident direction is negligible.

4.2 Suppressing Background Interference with Polarization Switching

Unlike active radios, the passive RoS tag reflects a similar amount of radar signal power as scattering objects in the environment, such as poles, pedestrians, trees, *etc.*. The background reflections can easily interfere with the desired tag reflection and compromise its detection performance. To address this challenge, we propose a polarization switching VAA (PSVAA) design. Most objects on the road barely impact the polarization of incidental signals upon reflection [18]. Our PSVAA is designed to switch the polarity of signals orthogonally to make the signals reflected by the tag stand out amid the background interference.

We construct the PSVAAs by extending the basic design in Section 4.1. Specifically, we rotate half of the patch antenna elements by 90° to create the second orthogonal polarization, as shown in Fig. 7a. A slight drawback of the PSVAA is that only half of the elements re-radiate, in contrast to the original VAA where a pair of connected elements radiate in a symmetric manner. Consequently, the power of the signal reflected by a PSVAA is halved, and the RCS is reduced by $20 \log_{10}(0.5) = 6$ dB. However, in Sec. 7.2, we show that the benefit from polarization switching is more than 14 dB, which sufficiently compensates for the RCS loss.

The PSVAA in RoS adopts a 4 layer PCB structure, as illustrated in the stackup in Fig. 7c. The top layer lays the patch antennas, followed by a ground layer below, a strip-line TL, and another ground layer. Next, we elaborate on the important design considerations.

(i) Substrate. We use two Rogers 4350B substrates ($\epsilon_r = 3.66$, $\tan\delta = 0.0037$) and a Rogers 4450F substrate ($\epsilon_r = 3.52$, $\tan\delta = 0.004$) to combine the two core layers. The material properties, ϵ_r and $\tan\delta$, define how the substrate interact with electromagnetic fields. The material loss parameter, $\tan\delta$, impacts the RCS of a PSVAA design and is chosen carefully based on extensive HFSS simulation under the constraint of the availability of substrates.
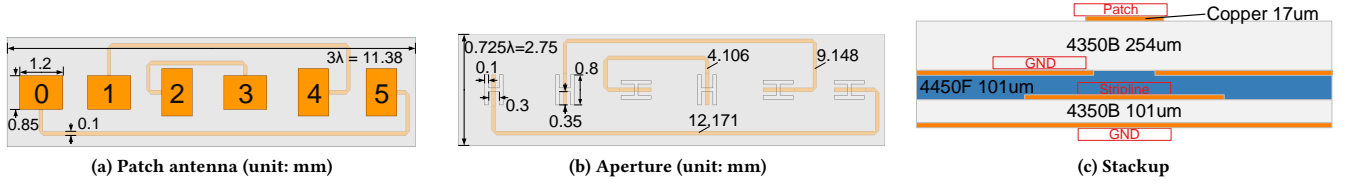
(a) Patch antenna (unit: mm)

(b) Aperture (unit: mm)

(c) Stackup

Figure 7: Structure of polarization-switched VAA (PSVAA).

(ii) Patch antenna. The PSVAA adopts rectangular *aperture coupled* patch antennas which use openings in ground planes to couple energy to the patch from a TL. The motivation behind this design choice was to hide the TLs in order to avoid spurious radiation that could interfere with the reflected signals as they travel down the line. An H-shaped aperture is used to couple the energy between the strip-line and patch antenna. Common aperture designs use slot openings but they generally have smaller coupling coefficients. By using large openings such as H or E shaped apertures, the coupling can be improved and the energy loss reduced. The aperture and patch dimensions are optimized using Ansys HFSS by performing parametric sweeps of the various dimensions. The optimization terminates when a return loss (*i.e.*, s_{11}) of -10 dB is achieved throughout the mmWave radar frequency band for the patch antenna. Fig. 7a and Fig. 7b shows the key geometrical parameters of the PSVAA, optimized for the 77-81 GHz band.

(ii) TL. The VAA model in Sec. 4.1 assumes only the patch antenna elements radiate signals. In practice, the TLs can also reflect the signals which reduces the retro-directive performance. We adopt strip-line TLs in the PSVAA design, which minimizes spurious radiation because they have smaller footprints and can be concealed by the two ground planes.

The geometrical design of the TLs follows Section 4.1, with a guided wavelength $\lambda_g = 2027$ μm at 79 GHz for the copper layer. We use HFSS again to optimize the length of the patch feed line coupling stub with an objective of maximizing the antenna gain while minimizing return loss. The TL lengths are determined by searching for the configuration that ensures the TL phase through the lines become equal at 79 GHz. As shown in Fig. 7b, the optimized coupling stub comes out to be 837.5μm terminating at 25μm from the edge of the patch, and the lengths of the three TLs are 4.106mm, 9.148mm, and 12.171mm, respectively. The lengths of the 2nd and 3rd TLs differ from the 1st by approximately 2.5λ_g and 4λ_g. The additional 0.5λ_g of the 2nd TL is used to remove the 180° phase offset induced by the difference of feeding directions between antennas with the same polarization. For example, as shown in Fig. 7a, the 2nd patch is fed from the left while the 4th patch is fed from the right, which induces a 180° phase shift between them. The polarization orders of the patches in Fig. 7a reduces the overall lengths of TLs and leads to a more compact design, as shown in Fig. 7b.

We verify the RCS performance of the PSVAA design in a similar way to Section 4.1. Fig. 5a compares the simulated RCS of the PSVAA and the original VAA, where the radar Tx and Rx antennas have orthogonal polarizations. The PSVAA achieves an RCS of around -43 dBsm for the orthogonally polarized return signal with a flat FoV of 120°, in contrast to around −55 dBsm for the original VAA. This
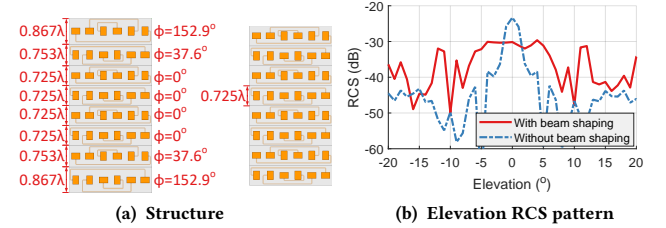

(a) Structure

(b) Elevation RCS pattern

Figure 8: Comparison between PSVAA stacks with and without beam shaping. In (a), left: with beam shaping, right: without beam shaping.

12 dB difference confirms that the PSVAA switches the polarization while maintaining a high RCS compared to the original VAA. Fig. 5b shows that for the original radar antennas without polarization switching, the PSVAA acts as a normal specular reflector, where only specular reflection at the norm direction can be received by the radar. We further simulate the RCS performance of the PSVAA across the 77-81 GHz band. As shown in Fig. 6a, the RCS of the switched polarization varies by less than 4dB, thanks to a return loss of over -10 dB. In contrast, as shown in Fig. 6b, the specular reflection introduces a strong main lobe and various side lobes across the frequency band, which are filtered out with the PSVAA. The results demonstrate the wide working bandwidth of the PSVAA.

4.3 Combating Height Mismatch Using Elevation Beam Shaping

The PSVAAs are retro-directive within the azimuth plane, but not in elevation. Rather, when stacked vertically for spatial encoding, multiple PSVAAs together create an unwanted elevation beamforming effect leading to an extremely narrow beamwidth. So even minor height misalignment between the radar and tag can weaken the RCS significantly.

Specifically, the beamwidth in radians of a vertically stack array of antennas can be calculated as follows [9]:

$$W = \frac{0.886\lambda}{2Nd_v} \tag{5}$$

where N is the number of antennas and d_v is the spacing between the centers of adjacent antennas. When stacking 32 PSVAAs vertically, the beamwidth would be 1.1°. At a distance of 3 m, the radar-tag height mismatch cannot exceed $3 \cdot \tan 0.55^o = 3$ cm! This is impractical in the automotive environment where the radar height varies depending on vehicle models and road conditions.

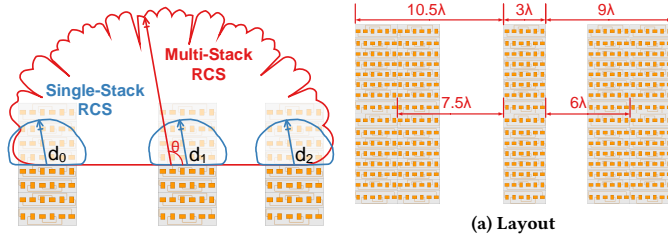To ensure a stable signal level in spite of the height mismatch,

(a) Layout

(b) RCS

(c) RCS Frequency Spectrum

Figure 9: RCS model.

Figure 10: An example 4-bit tag with 4 coding stacks and 1 reference stack of PSVAAs.

one solution is to design 2-D PSVAAs which connect the pairs of centrosymmetric antennas and are thus retro-directive in the elevation direction as well. However, this requires long TLs which incurs signal losses and lowers the RCS. For example, to connect the farthest centrosymmetric antenna pair in Fig. 12a, a 10.8 cm long TL is required, which induces a 11 dB loss given the material selection in Sec. 4.2. Such a large TL loss makes the antenna pair unusable. In addition, 2-D VAAs complicate the routing of the TLs compared with 1-D VAAs, potentially requiring many more PCB layers. Instead of the 2-D PSVAA, we design an elevation beam shaping scheme for 1-D PSVAAs arrays. The shaping broadens the elevation radiation pattern of the tag, which stabilizes the RCS as the radar's height varies.

Specifically, we treat each PSVAA in a vertical stack as a single "antenna element". We then find a set of phase weights for the "elements", which together lead to a flat-top radiation pattern. To apply a specific phase weight to a PSVAA, we increase the length of all three TLs. By adding $\frac{\phi}{2\pi}\lambda_g$ of TL length, a phase shift ϕ is introduced to the reflected signal relative to the baseline design in Section 4.2. Notably, the added TL length increases the height of each PSVAA. For a given set of phase weights, the relative positions of PSVAAs need to be adjusted accordingly to avoid overlapping. The position change in turn causes additional changes in the relative phases of PSVAAs. In other words, the desired phase weight of a PSVAA is a function of the weights of other PSVAAs. Such convoluted dependencies cannot be represented using closed-form analytical models.

To overcome this, we use a differential evolution genetic algorithm (DE-GA) [55], as a meta-optimization scheme to search for the phase weights and vertical positions of the PSVAAs, in order to achieve a desired wide elevation beamwidth (e.g., 10°). Fig. 8a (left) shows the optimized geometrical layout of an example stack of 8 PSVAAs, in contrast to the original design without elevation beam shaping (right). The polarization of the patches is altered between adjacent PSVAAs throughout the stack to ensure an overall symmetric RCS pattern. Fig. 8b further verifies that the corresponding elevation beam shape is flatten to around 10° (from 2°) and maintains a symmetric pattern.

5 EMBEDDING INFORMATION IN THE ROS TAG

RoS is designed as a passive, chipless and reconfigurable road sign for automotive mmWave radars. To avoid expensive and power-demanding mmWave circuit components, the RoS tag only consists of multiple PSVAA stacks. A straightforward encoding scheme

is to form an array of PSVAA stacks that creates a beam pattern with multiple lobes pointing to prescribed directions within the azimuth plane. A radar passing by can detect the directions of these beams and decode the embedded traffic sign information. However, a PSVAA is 3λ wide along the horizontal direction to accommodate multiple pairs of antenna elements and achieve retroreflection. Such a width is 12 times larger than the maximum horizontal spacing (i.e., $\frac{\lambda}{4}$) that avoids angular ambiguity of the array. As a result, with one coding beam formed by the array of PSVAAs, at least 11 ambiguous ambiguous beams are created, limiting the encoding angular range and reducing the peak power of the coding beam. Moreover, strong side lobes due to imperfection of the array may distort the pattern and interfere the decoding process.

To overcome the limitations of the above beam pattern based encoding scheme, RoS adopts a model-driven spatial encoding scheme. It directly encodes information bits using the layout of the PSVAA stacks. A radar can measure the RCS of the tag, from which it estimates the spatial layout and hence decodes the information bits. With such spatial coding, RoS can configure the information bits at fabrication time by altering the number of PSVAA stacks and adjusting their placement. In this section, we first model the RCS of an RoS tag, and then introduce the spatial encoding scheme that builds upon the RCS model. Finally, we discuss the practical constraints of the RoS tag.

5.1 RCS Model for Multi-Stack PSVAAs

Similar to a phased array with multiple antennas, the superimposed RCS of multiple PSVAA stacks is determined by their individual RCS and relative positions. Suppose that M stacks are linearly placed and the k-th stack is located at d_k, as shown in Fig. 9. The signal reflected by the k-th stack will experience a phase shift due to its round-trip propagation delay of $2d_k \cos\theta$, where θ is the signal's direction of arrival (DoA). Let $u = \cos\theta$, and denote λ as the signal wavelength in free space. The multi-stack RCS at DoA θ is then given by:

$$r_S(\theta) = \left| \sum_{k=0}^{M-1} \sqrt{r_T(\theta)} e^{i2\pi \frac{2d_k}{\lambda} u} \right|^2$$

$$= r_T(\theta) \sum_{k,l=0}^{M-1} e^{i4\pi \frac{d_k - d_l}{\lambda} u} \qquad (6)$$

$$= r_T(\theta) \left(M + 2 \sum_{k<l} \cos\left(4\pi \frac{d_k - d_l}{\lambda} u \right) \right),$$

where $r_T(\theta)$ is the RCS of the single-stack along DoA θ.

(a) Scene   (b) Point cloud   (c) Object RSS   (d) Frequency spectrum of RSS
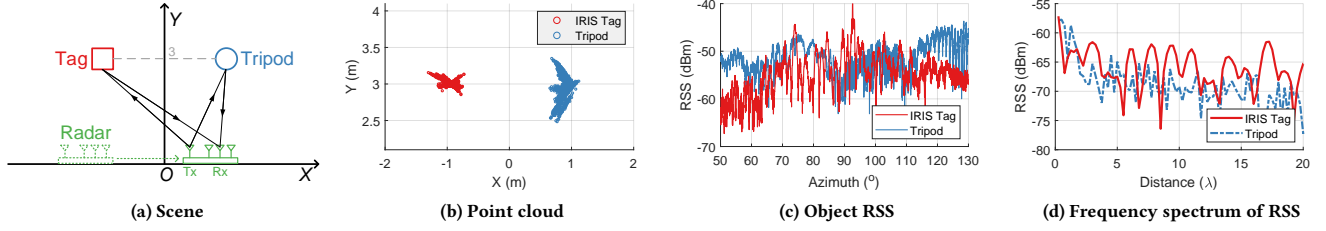
Figure 11: Illustration of detecting and decoding RoS tags with mmWave radar.

According to Eq. (6), the multi-stack RCS is the sum of cosines of the spacings between the individual stacks. Each cosine term can be viewed as a single tone at frequency $\frac{|d_k - d_l|}{0.5\lambda}$. We perform a Fourier Transform over u, and define the result as the *RCS frequency spectrum*:

$$R_S(v) = R_T(v) * \left(M + \sum_{k \neq l} \delta \left(v - \frac{d_k - d_l}{0.5\lambda} \right) \right), \qquad (7)$$

The Dirac Delta function $\delta(x)$ peaks at $x = 0$. Therefore, *the spacing between any two stacks, $d_k - d_l$, can be resolved by identifying the peak position $\frac{d_k - d_l}{0.5\lambda}$ in the frequency spectrum $R_S(v)$.* Since $u \in [-1, 1]$ has a range of 2, the frequency resolution of $R_S(v)$ is $\frac{1}{2}$. Also note that the spacing between stacks is proportional to the frequency v with a scaling factor of $\frac{1}{0.5\lambda}$. The resultant spacing resolution is as small as 0.25λ (*e.g.*, 0.95 mm for 79 GHz signals). In other words, we can *map the geometrical layout of the multi-stack PSVAAs to the RCS frequency spectrum, with sub-wavelength spatial resolution!*

5.2 Spatial Coding

While M PSVAA stacks have $M(M - 1)$ pairwise spacings, they are mutually dependent and can be uniquely determined by a set of $M - 1$ values. For example, given $\{d_k - d_0\}_{k=1}^{M-1}$, the relative location between an arbitrary pair of stacks (*e.g.*, k-th and l-th) can be calculated as $d_k - d_l = (d_k - d_0) - (d_l - d_0)$. We term the 0-th stack with $d_0 = 0$ as the *reference stack* and the rest as the *coding stacks*. Thus, *M stacks of PSVAAs can convey at most $M - 1$ independent coding bits, corresponding to $M - 1$ peaks in the RCS frequency spectrum.* Position of each peak is determined by the relative location between one coding stack and the reference stack, *i.e.*, $d_k - d_0$. *We use the presence (bit "1") or absence (bit "0") of each coding stack to encode information. With a maximum of M stacks on the tag, $M - 1$ bits can be encoded.*

Unfortunately, according to Eq. (6), the $M - 1$ frequency peaks at $\{\frac{|d_k|}{0.5\lambda}\}_{k=1}^{M-1}$ designated for coding may collide with the rest $(M - 1)^2$ secondary frequency peaks created by pairs of coding stacks. For example, given two coding peaks at $d_1 = \lambda$ and $d_2 = 2\lambda$, a secondary peak at $d_2 - d_1 = \lambda$ also appears and causes interference with the coding peak at $d_1 = \lambda$. To avoid such interference, we *separate the coding peaks from the secondary peaks in the frequency domain*. Specifically, we set the spacing between adjacent coding stacks to be equal, and place the k-th coding stack at $d_k = s_k(M + k - 2)\delta_c$, where δ_c is the basic unit spacing between coding stacks. The sign $s_k \in \{1, -1\}$ indicates whether the k-th stack is on the left side (*i.e.*, $s_k = -1$) or the right side (*i.e.*, $s_k = 1$) of the reference stack.

Therefore, the distance between any k-th and l-th coding stacks on the same side of the reference stack satisfies $|d_k - d_l| < d_1$, while those on different sides should have $|d_k - d_l| > d_{M-1}$. Consequently, all the secondary peaks are out of the coding band from d_1 to d_{M-1} where the coding peaks are located.

To verify the design, we conduct 3D EM field simulation in HFSS for an example tag with $M = 5$ and $\delta_c = 1.5\lambda$. Fig. 10 shows the layout, RCS, and the RCS frequency spectrum of the tag. The 4 coding stacks are placed at 6λ, -7.5λ, 9λ and -10.5λ relative to the reference stack. We see that 4 prominent peaks appear at the locations of the coding stacks encoding 4 bits "1111". All the secondary peaks are separated from the coding peaks in frequency and can be omitted. Note that the RoS tag can be easily configured to encode other bits by adding or removing coding stacks. For example, to encode bits "1010", we can simply remove the two stacks at -7.5λ and -10.5λ in Fig. 10.

5.3 Modeling Performance Limit and Design Tradeoffs

Encoding capacity. Given a tag with $M - 1$ coding bits and a $\delta_c = c\lambda$, the width of the tag, D, can be calculated as, $D = |d_{M-1}| + |d_{M-2}| + 3\lambda = ((4M - 7)c + 3)\lambda$. Two factors limit D and ultimately the number of coding bits (*i.e.*, $M - 1$) that a single tag can achieve. *First*, the above multi-stack RCS model assumes that the radar is within the far field region of the tag where propagation paths from the PSVAA stacks to the radar are approximately parallel, *i.e.*,

$$d \geq \frac{2D^2}{\lambda}, \qquad (8)$$

where d is the radar-to-tag distance. *Second*, the maximum frequency peak appears at $\frac{D}{0.5\lambda}$. Since the radar is moving, two consecutive radar frames are collected at different locations. Suppose their spatial interval is δ_s. According to the Nyquist sampling theorem, δ_s should satisfy:

$$\sin \frac{\delta_s}{d} \leq \frac{2\lambda}{0.5D}. \qquad (9)$$

An example tag with 4 coding bits in our RoS implementation is shown in Fig. 10. With a tag width of $D = 22.5\lambda$, the far field distance of the tag would be $d = 2.9$ m according to Eq. (8) . Therefore, the spatial encoding is most effective when the tag-to-radar distance exceeds 2.9 m. Denoting the radar frame rate by F_s, the maximum vehicle speed v supported by the tag is $v = \delta F_s \approx \frac{4d\lambda F_s}{D}$ according to Eq. (9). Modern mmWave radars (*e.g.*, the TI radar [22]) can easily achieve $F_s \geq 1$ kHz. Ideally, the tag can be decoded when the moving speed of the vehicle is below 38.5 m/s (*i.e.*, 86 mph).

If more than 4 bits are encoded within a single tag, the far field distance is extended farther which in turn requires higher radar sensitivity. For example, for a tag with 6 coding bits and a spacing $\delta_c = 1.5\lambda$, the tag width is $D = 34.5\lambda$. The far field distance would be 9 m. To encode more bits at practical distances, RoS can instead place multiple tags side by side similar to advertising boards. This would require that the radar isolates the signals from adjacent tags, *i.e.*, two tags having an angular separation larger than the radar's half beam width, *i.e.*, $1/N_a$, according to Sec. 3.2. Typical mmWave radars, such as the TI radar, have at least $N_r = 4$ Rx antennas. The minimum distance between two tags at $d = 6$ m should be at least 1.53 m following trigonometry.

Link budget and detection range. According to Eq. (1), the communication distance d between the radar and the tag is $d = \left(\frac{P_t G_t G_r \lambda^2 \sigma}{(4\pi)^3 P_r}\right)^{1/4}$. To decode the tag, the RSS at the radar should exceed the noise floor, *i.e.*, $P_r \geq L_o$ which limits the maximum communication distance of the tag. The noise floor is calculated as $L_o = c_0 N_{NF} B_{IF} G_{ra} G_{rs}$, where $c_0 = -173.9$ dBm is the thermal noise constant; $N_{NF}, B_{IF}, G_{ra}, G_{rs}$ are the noise figure, intermediate frequency (IF) bandwidth, the receive antenna gain, and the signal processing gain by combining multiple antennas. Specific to our implementation, on the dB scale, the TI radar [22] has $N_{NF} = 15$ dB, $B_{IF} = 37.5$ MHz, $G_{ra} = 9$ dB and $G_{rs} = 12$ dB with 4 receive antennas. With that, the minimum RSS level is $P_r = -62$ dBm. Given that the RCS of an RoS 32-array tag is $\sigma = -23$ dBsm according to the Ansys HFSS simulation result, and that the TI radar has a radar EIRP of $P_t + G_t = 21$ dBm, an Rx gain of $G_r = G_{ra} + G_{rl} + G_{rs} = 55$ dB, where $G_{rl} = 34$ dB, then the maximum achievable distance is $d \approx 6.9$ m which covers vehicle radars approximately two roadway lanes away from the tag.

6 INTERROGATING THE ROS TAG WITH AN AUTOMOTIVE RADAR

A vehicle passing by an RoS tag can measure its RCS, convert it into the RCS spectrum $R_S(v)$ (Sec. 5.1), and decode the embedded information following Sec. 5.2. Traditionally, RCS measurements are conducted to measure the electromagnetic signatures of objects. Thus, it is usually controlled in an anechoic chamber where the transceiver is fixed and the object rotates at a constant speed [12]. In contrast, RoS works in the more dynamic and open driving scenario. The relative location/orientation between the radar and the tag may continuously change, which renders the traditional RCS measurement procedure infeasible. In addition, RoS has to discriminate the signals reflected by the tag in the presence of irrelevant objects. Fig. 11a illustrates a typical scenario with two tripods where one of them is mounted with a tag. We use this setup as an example to showcase how the radar can accurately sample the tag's RCS in RoS.

To measure the RCS of roadside objects, RoS uses the radar to continuously localize them. Meanwhile, the radar applies beamforming with the polarization switched Tx antenna to obtain reflection signal strengths across different angles. Specifically, for each radar frame, RoS uses the standard processing flow in Sec. 3.2 (also c.f. [42]) to generate a point cloud representing the dominant reflectors visible to the radar. After all frames are processed, RoS merges their point clouds based on the *relative* radar locations where the
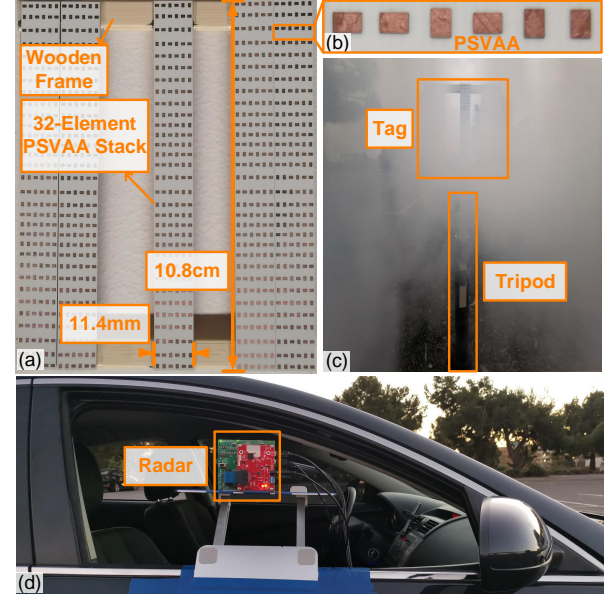

Figure 12: Experimental setup. (a) RoS tag. (b) A single PSVAA on the tag. (c) RoS tag in heavy fog condition. (d) TI radar mounted on the test vehicle.

frames are transmitted. Such relative location information can be easily obtained by interpolating the measurements from the inertial motion sensors and speed sensors on board. Intuitively, dominant reflectors are visible in most frames and their points tend to be dense. Thus, RoS applies the classical density-based clustering algorithm, *i.e.*, DBSCAN [15], to cluster the points. It calculates the point density of each cluster and keeps those with density larger than a predefined threshold for further RCS measurement. Specific to our example setup, Fig. 11b shows the two clusters representing the tag and the tripod with prominent point densities.

For each cluster, RoS calculates its center of gravity and assigns it as the location of the corresponding object. Now that the relative location between the object and the sampling position of each radar frame is known, RoS applies beamforming weights to the returned signals to "spotlight" on each object and estimate its total RSS contribution. Such beamforming mechanism is a standard practice in MIMO radar [42]. The RSS reflected from the RoS tag and the tripod in our experiment are shown in Fig. 11c.

We further leverage two representative features to differentiate the RoS tag from other objects on the road to avoid misdetection. First, as different types of objects vary in size, we calculate the sizes of the point clusters corresponding to the objects. Second, while most objects on the road reflect signals with the original polarization, RoS changes the polarization of the reflected signals. Since RoS tags tend to have a smaller RSS loss of the polarization switching Tx relative to the original Tx of the radar, we can use the calculated RSS loss as a second feature. In Sec. 7, we show that the features of RoS tags are statistically different from the other rod-shaped objects on the road, verifying the effectiveness of using the two features to detect RoS tags.

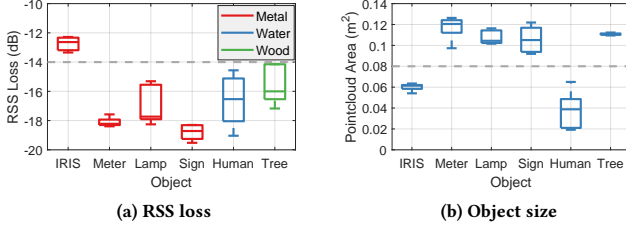Now that the tag's RSS contribution can be isolated from other

(a) RSS loss

(b) Object size

Figure 13: Performance of tag detection.

(a) RSS

(b) SNR

Figure 14: Effectiveness of elevation beam shaping.

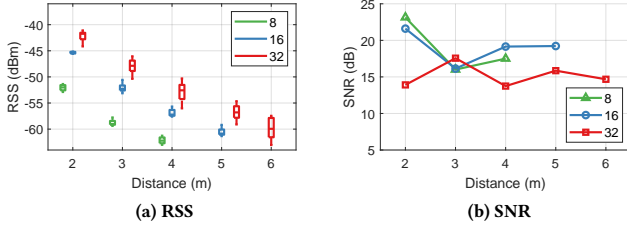
(a) RSS

(b) SNR

Figure 15: Impact of radar-to-tag distance.

objects, and the RSS is equivalent to a scaled version of RCS (Eq. (1)), *we can directly apply an FFT to the tag's RSS to generate its RCS frequency spectrum.* Finally, the coding peaks are normalized by the overall power within the coding band and detected and decoded following the model in Sec. 5.1. Taking the 4-bit tag in Fig. 10a as an example, we show the measured frequency spectrum of the tag and the tripod's RSS in Fig. 11d. The measured RSS frequency spectrum of the tag has 4 coding peaks around 6, 7.5, 9, 10.5λ, which match the ones in the simulated RCS frequency spectrum in Fig. 10c.

7 EVALUATION

7.1 Experimental Method

Implementation. We fabricate RoS tags following the standard PCB production process. Stacks with different number of beam-shaped PSVAA are designed in HFSS and imported into Altium Designer to generate PCB design files. Although our PSVAA design can filter out environmental reflections, large objects that are extremely close to the tag may still leak reflections into the orthogonal polarity and interfere with the tag's response. Our initial setup mounted the tag on a basal wood board which has a much larger electronic signature causing interference. Therefore, we replaced the board with a wooden frame which has a smaller cross sectional area, thus reducing the interference and improving SNR. Fig. 12a shows an example assembled tag, which has 5 vertical stacks and encodes 4 bits "1111". Each stack has 32 PSVAAs. The stacks can be reconfigured to encode different bit sequences following Sec. 5.2.

The radar's Tx and Rx antennas should have orthogonal polarization directions to receive backscattered signals from PSVAAs. Typical patch antennas are linearly polarized, just like the TI radar used in our experiments, so we simply rotate one Tx or Rx antenna by 90° to achieve an orthogonal polarity. The radar's front-end hardware schematics [22] remain intact. Note that if the antenna with the original polarity is still desired, one can simple add a polarized antenna and use an RF switch to toggle between the two.
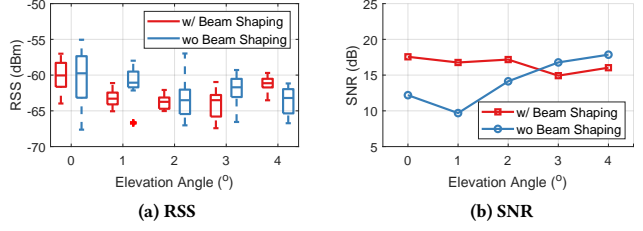
Evaluation setup. We assemble RoS tags with different coding bits, attach the tags to a tripod and place it on the roadside for measurement. By default, we set the TI radar's parameters as follows: frame duration 60 μs, frame repetition rate F_s = 1 kHz, frequency slope 66 MHz/μs, baseband sampling rate 5 Msps, and the number of samples per frame equals 256. The radar uses one original Tx antenna for object detection and the polarization switching Tx antenna for tag decoding. 4 Rx antennas are used to achieve a beamwidth around of 28.6°. To control the variables in the micro-benchmark experiments, the radar was mounted on a cart and manually moved. A stereo camera [54] was co-located with the radar to obtain its ground truth positions relative to the tag. To evaluate system robustness against adverse weather, a fog generator [11] is used to emulate real fog, as shown in Fig. 12c. For field testing under vehicle speed, we further mounted the radar on a sedan (Fig. 12d) which moved along straight trajectories passing by the RoS tag.

Evaluation metrics. RoS encodes bit "1" with peaks and bit "0" with nulls in the RCS spectrum which can be considered an on-off keying (OOK) modulation scheme. Directly computing bit error rate (BER) of the decoding scheme entails repeating the drive-through experiments millions of times which is infeasible. We thus measure the SNR of the coding peaks and then convert it to BER. Intuitively, coding peaks with higher SNR are more prominent, and thus easier to be correctly decoded. Specifically, the SNR equals $(\mu_1 - \mu_0)^2/\sigma^2$, where μ_i is the average amplitude of bit "i" and σ is the standard deviation of the coding peak amplitudes. The SNR to BER mapping follows the OOK model where BER = $\frac{1}{2}\text{erfc}(\sqrt{\frac{\text{SNR}}{8}})$ [56]. As an example, a 15.8 dB SNR corresponds to a BER of 0.1%.

7.2 Performance of RoS Tag

Tag detection. Recall that RoS uses the polarization suppression and point cloud size as features to discriminate the tag from other objects (Sec. 6). To verify this approach, we place the RoS tag on the roadside with common objects nearby, *e.g.*, parking meter, street lamp, ordinary road signs, pedestrian and trees, which are less than 0.5 m from the tag. The minimum distance of the radar is 3 m as it passes by the tag. Fig. 13a shows the RSS loss achieved by the polarization switching mechanism (Sec. 4.2). While background objects more or less affect the polarization of reflected signals, they experience a median RSS rejection of 16-19 dB. In contrast, the median RSS loss of the RoS tag is only around 13 dB, implying that the tag-reflected signals tend to be much stronger than background reflections. Fig. 13b further shows that the point cloud size of the
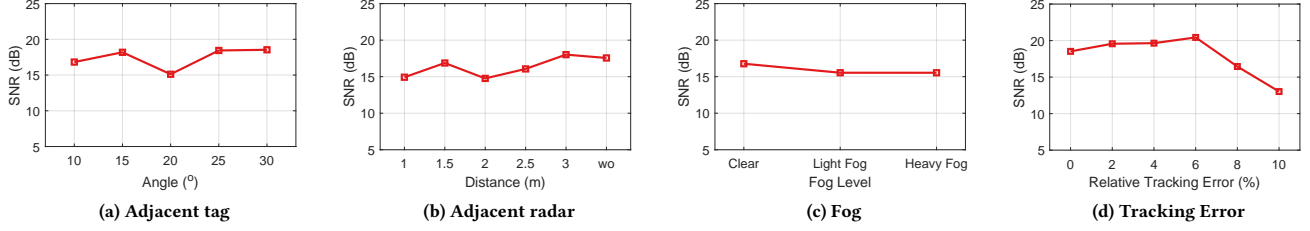
(a) Adjacent tag   **(b) Adjacent radar**   **(c) Fog**   **(d) Tracking Error**

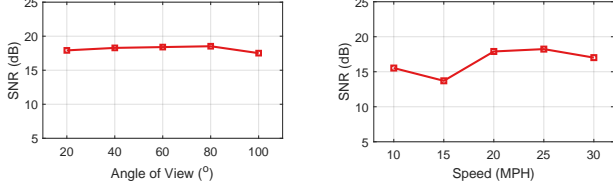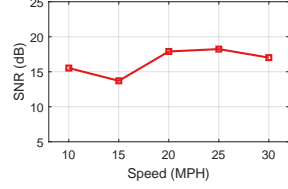**Figure 16: Impact of interference.**

Figure 17: Impact of angular FoV.   **Figure 18: Impact of vehicle speed.**

RoS tag is much smaller than all other objects except pedestrians, so it represents an effective feature to discriminate the tags. *Owing to the two discriminative features, i.e., higher RSS and smaller point cloud size, RoS can correctly identify the tags without any miss detection or false alarm in all our tests.* Note that the objects with sufficient separation from the tag do not usually interfere with RoS decoding, because they can be easily discriminated in the radar point cloud.

Effectiveness of elevation beam shaping. To verify the beam shaping design (Sec. 4.3), we fix the radar 3 m away from the tag and vary its vertical position to create height (and elevation angle) misalignment. To create baseline tags without beam shaping, we stack multiple VAAs with zero phase offset (*i.e.*, equal vertical distance) and ensure the stacks are positioned in the same way as those on our elevation beam shaping tag.

As shown in Fig. 14a, the RSS of the baseline tags decreases as the elevation misalignment increases while that of the RoS tags is more consistent. However, the decreasing trend is not monotonous, as the radar happens to fall in the main beam of some coding stacks of the baseline tags and receives high RSS. It is possibly due to tag height mounting errors, tag swaying caused by wind, or bending of long coding columns, which are unavoidable in outdoor settings. In addition, the baseline tags exhibit wild RSS variation. For example, the RSS varies by 13 dB when the tag and the radar are placed at the same height. The main reason is that the baseline tags only have an elevation beamwidth of $1.27°$ so even minor inadvertent misalignment can impact the RSS significantly. Fig. 14b shows the corresponding SNR of the coding bits. With beam shaping, the SNR of the RoS tags remains over 15 dB (*i.e.*, BER above 0.3%), thanks to their consistently small RSS variance. In contrast, the baseline tags achieve an SNR as low as 10 dB (*i.e.*, BER 5.7%), making the detection much less robust.

In summary, *with elevation beam shaping, the RoS tags work reliably even at ±4° of elevation angle deviation.* This corresponds to a tolerable height mismatch of 28 cm even when the radar-to-tag distance is close to 2 m. The tolerance increases with distance and with a wider elevation beam.

Impact of distance. In practice, vehicles may pass by a RoS tag across different lanes corresponding to different radar-to-tag interrogation distances (Fig. 1). We evaluate the impact using 3 types of tags with 8, 16, and 32 PSVAAs per stack. Fig. 15a shows that the RSS decreases over distance following the path loss model (Eq. (1)). The tags with 8, 16, and 32 PSVAAs per stack cannot be detected beyond 4, 5, and 6 m respectively as their RSS drops near the noise floor of the TI radar. Thus, different types of tags can be deployed depending on the number of lanes on the road. Fig. 15b shows the corresponding SNR. While the SNR of all tags remains above 14 dB (*i.e.*, a BER of 0.6%), the 8-array and 16-array tags have statistically higher SNR than the 32-array tags. The main reason lies in the longer far field distance of the 32-array. Specifically, as shown in Fig. 12a, the height of a 32-array PSVAA stack is about 10.8 cm, corresponding to a far field distance of 6.14 m following Eq. (8). In contrast, the far field distance is 0.31 m and 1.36 m for the 8- and 16-array tags respectively. In other words, in most of the test cases (1-6 m range), the 32-array tags only work in its near field where the spatial encoding model is inaccurate, which causes the SNR degradation.

7.3 Practical Vehicular Scenarios

Multi-tag and multi-radar interference. Recall that we can place multiple RoS tags side by side to encode more data bits. To evaluate the cross-tag interference, we place two tags 3 m away from the radar and adjust their separation so that their spread angle viewed by the radar ranges from $10°$ to $30°$. Fig. 16a shows that the SNR of the tags only slightly increases with the increase of their spread angle, indicating the interference between tags is negligible.

In addition, two vehicles can simultaneously interrogate the same tag as they pass by as long as the tag is within FoV of the vehicles. To examine the potential interference, we repeat the decoding experiment with 2 TI radars. The spacing between the radars varies from 1 to 3 m with a step of 0.5 m to account for realistic separation between adjacent vehicles. Fig. 16b shows that the tag SNR slightly increases with larger separation between the radars. Nonetheless, the SNR remains above 15 dB even at an extremely close separation of 1 m. The reasons are two fold. First, due to the PSVAA design, the RoS tag retroreflects signals back to the source and thus suppresses the interference between radars (see Fig. 4). Second, while other surrounding objects may create specular reflections between radars, such interference is transient in the angular domain and only slightly raises the noise floor in the frequency domain. Since RoS encodes bits in the frequency domain, these specular reflections have little impact on it. However, detection and decoding of

a RoS tag fails when it is fully blocked by another vehicle, since mmWave signals cannot penetrate metal. Chances of full blockage can be reduced by mounting RoS tags higher than the vehicles and installing redundant RoS tags along the road.

Detection under foggy weather. Compared to vision sensors such as camera and lidar, radar is robust under adverse weather conditions such as fog, rain and snow. For example, the attenuation at 79 GHz due to heavy fog (water droplet concentration equals 1 mg/m^3) is about 2 dB per 100 m [4] while that due to heave rain (precipitation 100 mm/h) is only slightly higher (3.2 dB per 100 m) [64]. Existing work has leveraged such properties to complement cameras and enable point cloud generation under adverse weather [43]. To showcase RoS under adverse weather conditions, we use a fog generator [11] to emulate fog at different levels, as shown in Fig. 12c. In Fig. 16c, it is observed that the median SNR remains above 15 dB (*i.e.*, a BER of 0.3%) across all fog levels, demonstrating the robustness of RoS against fog.

Impact of tracking error. Even though modern vehicles are equiped with a variety of location-tracking equipment (camera, Lidar, IMU, *etc.*), the self-tracking errors seem to be inevitable. To evaluate its impact on tag decoding, we add relative drifting errors from 2% to 10% with a step of 0.2 m to the ground truth tracking data. Fig. 16d shows that the SNR remains around 20 dB when the relative tracking error is less than 6%, and decreases with larger tracking error, mainly due to the distortions of the coding peaks in the RCS frequency spectrum. Fortunately, using IMU sensors and speedometers, existing works [60, 61] can track vehicles accurately with small drifting errors (e.g., $\leq$ 2%), which easily achieves the tracking accuracy required by RoS.

Impact of angular field of view (FoV). While the theoretical maximum angular FoV of a RoS tag is 180°, it cannot be achieved in practice due to two limitations. First, the retroreflective beamwidth of a VAA is around 100° as shown in Fig. 4a, and that of a typical radar antenna is only around 60° [22]. Second, as a vehicle radar moves along a straight line, the viewing angle is limited by the maximum detectable distance of the tag. To better understand the impact, we manually truncate the RCS to a limited FoV from 20° to 100°. Fig. 17 shows the SNR of coding peaks with different angular FoV. The impact of the angular FoV is minor. The decoding SNR slightly increases when the angular FoV increases from 20° to 80°. Theoretically, with a FoV larger than 60°, the location resolution is finer than $\frac{\lambda}{2 \cdot 2 \sin 30^o} = 0.5\lambda$, and the coding peaks can be clearly separated in the frequency spectrum of RCS. The decoding SNR slightly decreases when the angular FoV reaches 100°. It is mainly due to the RCS measurements outside of the FoV of the radar, which are dominant by noises and raises the noise floor of the frequency spectrum of the RCS. The result indicates that an angular FoV of 60° is sufficient to decode RoS tags. As the maximum detection distance of a tag is 6 m using the TI radar, it only requires that the vehicles move across a trajectory of at most 6 m when passing by the tag, so as to sample the RCS across 60°.

Impact of vehicle speed. We mount the radar on a vehicle moving at 10 to 30 mph with a 5 mph step. Fig. 18 shows the SNR measured at different driving speeds. The large variation across different speeds is mainly due to the more dynamic driving condition compared with the case where the radar is mounted on the cart.

Despite this, the decoding SNR consistently exceeds 14 dB (*i.e.*, a BER of 0.6%), demonstrating the effectiveness of the tag decoding in practical driving scenarios. While high speeds lead to prominent Doppler effect, the Doppler frequency shifts (e.g., 19 kHz at a speed of 80 mph) are orders of magnitude smaller than the carrier frequency of mmWave signals (i.e., 79 GHz), and have little impact on the RCS pattern, as validated by the consistent SNR in Fig. 18.

8 DISCUSSION AND FUTURE WORK

Extending the detection range. The TI radar in our experiments is intended as a development board with limited transmit power, antenna gain and high receiver noise figure [22], which largely limits the detection range. Fortunately, commercial automotive radars have much better performance. With a low noise figure of N_{NF} = 9 dB [34], and EIRP of $P_t + G_t$ = 50 dBm in the 76-81 GHz band [36], a maximum distance of 52 m can be achieved according to Sec. 5.3. The range can be further improved by overcoming the 6 dB RCS loss of the PSVAA with circularly polarized (CP) antenna elements [19]. While common objects change the left/right-hand direction of circular polarized signals upon reflection, the PSVAA with CP antennas does not, enabling the radar to separate the reflections without the 6 dB loss.

Increasing the encoding capacity. The current RoS prototype has limited encoding capacity due to the near-far field tradeoff (Sec. 5.3), *i.e.*, encoding more bits requires further tag-to-radar separation which in turn reduces RCS. By using near-field-focusing-antennas (NFFA) [6], the requirement can be relaxed. That is, a larger tag encoding more bits can be decoded by a radar within the near field. Larger encoding capacity also allows for error correction mechanisms to improve the reliability of decoding. In addition, with larger vertically stacked VAAs enabled by NFFAs, a higher RCS level can be achieved, which ultimately raises the SNR of coding bits and reduces the coding BER. The encoding capacity can also be improved through modulation schemes other than OOK. The RCS levels of each encoding bit "1" can be adjusted by varying the number of PSVAAs within a stack. Multiple RCS levels can enable ASK modulation which can improve the encoding capacity by multi-folds.

9 CONCLUSION

We have designed and validated RoS, a lightweight mechanism to smarten road infrastructure through reconfigurable, radar-readable signage. The RoS design can be generalized as a smart passive surface which acts as a mechanically reconfigurable "barcode" for RF interrogating devices, including not only radar, but also RF communication devices such as WiFi, DSRC, and WiGig. The RoS design can be extended to accommodate a wider range of use cases. We confirm this work does not raise any ethical issues.

ACKNOWLEDGMENTS

REFERENCES

[1] Omid Abari, Deepak Vasisht, Dina Katabi, and Anantha Chandrakasan. 2015. Caraoke: An e-toll transponder network for smart cities. In *Proceedings of ACM SIGCOMM*.

[2] Kashif Ali and Hossam Hassanein. 2009. Using passive RFID tags for vehicle-assisted data dissemination in intelligent transportation systems. In *IEEE Conference on Local Computer Networks*.

[3] Paris Ang and George V Eleftheriades. 2018. A passive redirecting Van Atta-type reflector. *IEEE Antennas and Wireless Propagation Letters* 17, 4 (2018), 689–692.

[4] Nezah Balal, Gad A Pinhasi, and Yosef Pinhasi. 2016. Atmospheric and fog effects on ultra-wide band radar operating at extremely high frequencies. *MDPI Sensors* 16, 5 (2016), 751.

[5] Isaac Balbin and Nemai Karmakar. 2009. Novel chipless RFID tag for conveyor belt tracking using multi-resonant dipole antenna. In *Proceedings of IEEE EuMC*. IEEE, 1109–1112.

[6] A Buffi, PAOLO Nepa, and GIULIANO Manara. 2012. Design criteria for near-field-focused planar arrays. *IEEE Antennas and Propagation Magazine* 54, 1 (2012), 40–50.

[7] Jitendra N Chourasia and Preeti Bajaj. 2010. Centroid based detection algorithm for hybrid traffic sign recognition system. In *Proceedings of IEEE ICETET*.

[8] Cincom. 2020. Cincomlighting. https://www.cimconlighting.com/.

[9] Balanis A. Constantine. 2016. *Antenna theory: Analysis and Design*. Wiley.

[10] Continental. 2020. Intelligent Intersection. https://www.continental.com/en/press/fairs-events/techshow-2019/intelligent-intersection-175910.

[11] Cozplace. 2021. Heavy Duty Fog Smoke Effect Generator. https://cozpalace.com/products/heavy-duty-fog-smoke-effect-generator-machine-sfm-0000-00

[12] N.C. Currie. 1989. *Radar Reflectivity Measurement: Techniques and Applications*. Artech House.

[13] Yury Y Danilov, Gregory G Denisov, Mikhail A Khozin, Alexander Panin, and Yury Rodin. 2014. Millimeter-wave tunable notch filter based on waveguide extension for plasma diagnostics. *IEEE Transactions on Plasma Science* 42, 6 (2014), 1685–1689.

[14] Arturo De la Escalera, J Ma Armingol, and Mario Mata. 2003. Traffic sign recognition and analysis for intelligent vehicles. *Elsevier Image and vision computing* 21, 3 (2003), 247–258.

[15] Martin Ester, Hans-Peter Kriegel, Jörg Sander, and Xiaowei Xu. 1996. Density-based spatial clustering of applications with noise. In *Proceedings of ACM KDD*.

[16] Chuhan Gao, Yilong Li, and Xinyu Zhang. 2018. LiveTag: Sensing human-object interaction through passive chipless WiFi tags. In *Proceedings of USENIX NSDI*.

[17] José Ramón García Oya, Rubén Martín Clemente, Eduardo Hidalgo Fort, Ramón González Carvajal, and Fernando Muñoz Chavero. 2018. Passive RFID-Based Inventory of Traffic Signs on Roads and Urban Environments. *Sensors* 18, 7 (2018). https://doi.org/10.3390/s18072385

[18] Angelos A Goulianos, Alberto L Freire, Tom Barratt, Evangelos Mellios, Peter Cain, Moray Rumney, Andrew Nix, and Mark Beach. 2017. Measurements and characterisation of surface scattering at 60 GHz. In *Proceedings of IEEE VTC-Fall*.

[19] Gerhard F Hamberger, Stefan Späth, Uwe Siart, and Thomas F Eibert. 2018. A mixed circular/linear dual-polarized phased array concept for automotive radar—planar antenna designs and system evaluation at 78 GHz. *IEEE Transactions on Antennas and Propagation* 67, 3 (2018), 1562–1572.

[20] Mehrdad Hessar, Ali Najafi, and Shyamnath Gollakota. 2019. Netscatter: Enabling large-scale backscatter networks. In *Proceedings of USENIX NSDI*.

[21] Jimmy GD Hester and Manos M Tentzeris. 2016. Inkjet-printed flexible mm-wave Van-Atta reflectarrays: A solution for ultralong-range dense multitag and multisensing chipless RFID implementations for IoT smart skins. *IEEE TMTT* 64, 12 (2016), 4763–4773.

[22] Texas Instruments. 2019. TI IWR1443 single-chip 76-GHz to 81-GHz mmWave sensor evaluation module. https://www.ti.com/tool/IWR1443BOOST

[23] Shinya Iwasaki, Chinthaka Premachandra, Tomohiro Endo, Toshiaki Fujii, Masayuki Tanimoto, and Yoshikatsu Kimura. 2008. Visible light road-to-vehicle communication using high-speed camera. In *IEEE Intelligent Vehicles Symposium*.

[24] I Jalaly and ID Robertson. 2005. Capacitively-tuned split microstrip resonators for RFID barcodes. In *Proceedings of IEEE European Microwave Conference*. IEEE.

[25] Amol Jayant Kale and RC Mahajan. 2015. A road sign detection and the recognition for Driver Assistance Systems. In *International Conference on Energy Systems and Applications*.

[26] Song Kunpeng and Feng Dejun. 2019. The Frequency-Shifting Modulation of Radar Signal Using Active Van Atta Array. In *Proceedings of IEEE ICSIP*.

[27] Kevin MKH Leong, Ryan Y Miyamoto, and Tatsuo Itoh. 2003. Moving forward in retrodirective antenna arrays. *IEEE Potentials* 22, 3 (2003), 16–21.

[28] Zhengxiong Li, Baicheng Chen, Zhuolin Yang, Huining Li, Chenhan Xu, Xingyu Chen, Kun Wang, and Wenyao Xu. 2019. FerroTag: a paper-based mmWave-scannable tagging infrastructure. In *Proceedings of ACM SenSys*.

[29] Zhuqi Li, Can Wu, Sigurd Wagner, James C. Sturm, Naveen Verma, and Kyle Jamieson. 2020. REITS: Reflective Surface for Intelligent Transportation Systems. arXiv:2010.13986 [cs.NI]

[30] Vincent Liu, Aaron Parks, Vamsi Talla, Shyamnath Gollakota, David Wetherall,

[31] and Joshua R Smith. 2013. Ambient backscatter: Wireless communication out of thin air. *Proceedings of ACM SIGCOMM* (2013).

[31] Mohammad Hossein Mazaheri, Alex Chen, and Omid Abari. 2020. Millimeter Wave Backscatter: Toward Batteryless Wireless Networking at Gigabit Speeds. In *Proceedings of ACM HotNets*. 139–145.

[32] Krzysztof Małecki and Kamil Kopaczyk. 2013. RFID-Based Traffic Signs Recognition System, Vol. 395. 115–122. https://doi.org/10.1007/978-3-642-41647-7_15

[33] Zhuo-Wei Miao, Zhang-Cheng Hao, and Quan Yuan. 2017. A passive circularly polarized Van Atta reflector for vehicle radar applications. *IEEE Antennas and Wireless Propagation Letters* 16 (2017), 2254–2257.

[34] Tomotoshi Murakami, Nobumasa Hasegawa, Yoshiyuki Utagawa, Tomoyuki Arai, and Shinji Yamaura. 2019. A 9 dB Noise Figure Fully Integrated 79 GHz Automotive Radar Receiver in 40 nm CMOS Technology. In *Proceedings of IEEE RFIC*. 307–310.

[35] Jeffrey A Nanzer. 2012. *Microwave and millimeter-wave remote sensing for security applications*. Artech House.

[36] Federal Communications Commission Office of Engineering and Technology Laboratory Division. 2019. Equipment Authorization Guidance for 76-81 GHz Radar Devices. (2019).

[37] Aritra Paul, R Jagriti, Nischit Bharadwaj, S Sameera, and Arjun S Bhat. 2011. An RFID based in-vehicle alert system for road oddities. In *2011 IEEE Recent Advances in Intelligent Computational Systems*. 019–024. https://doi.org/10.1109/RAICS.2011.6069265

[38] Stefano Pellerano, Javier Alvarado, and Yorgos Palaskas. 2010. A mm-Wave Power-Harvesting RFID Tag in 90 nm CMOS. *IEEE Journal of Solid-State Circuits* 45, 8 (2010), 1627–1637. https://doi.org/10.1109/JSSC.2010.2049916

[39] Stevan Preradovic and Nemai C Karmakar. 2009. Design of fully printable planar chipless RFID transponder with 35-bit data capacity. In *Proceedings of IEEE EuMC*.

[40] Stevan Preradovic and Nemai Chandra Karmakar. 2010. Chipless RFID: Bar code of the future. *IEEE microwave magazine* 11, 7 (2010), 87–97.

[41] Stevan Preradovic, Nemai C Karmakar, and Isaac Balbin. 2008. RFID transponders. *IEEE microwave magazine* 9, 5 (2008), 90–103.

[42] Kun Qian, Zhaoyuan He, and Xinyu Zhang. 2020. 3D Point Cloud Generation with Millimeter-Wave Radar. *Proc. ACM Interact. Mob. Wearable Ubiquitous Technol.* 4, 4, Article 148 (2020), 23 pages.

[43] Kun Qian, Shilin Zhu, Xinyu Zhang, and Li Erran Li. 2021. Robust Multimodal Vehicle Detection in Foggy Weather Using Complementary Lidar and Radar Signals. In *IEEE/CVF Conference on Computer Vision and Pattern Recognition, CVPR*.

[44] Yu-Jiun Ren and Kai Chang. 2007. A broadband van atta retrodirective array for ka-band applications. In *IEEE Antennas and Propagation Society International Symposium*.

[45] Yu-Jiun Ren and Kai Chang. 2007. A new millimeter-wave broadband retrodirective antenna array. In *IEEE/MTT-S International Microwave Symposium*. 1711–1714.

[46] Mark A Richards. 2005. *Fundamentals of radar signal processing*. Tata McGraw-Hill Education.

[47] Florian Alexander Schiegg, Nadia Brahmi, and Ignacio Llatser. 2019. Analytical Performance Evaluation of the Collective Perception Service in C-V2X Mode 4 Networks. In *Proceedings of IEEE ITSC*.

[48] Yousuf Shafiq, John S Gibson, Hyun Kim, Cedric P Ambulo, Taylor H Ware, and Stavros V Georgakopoulos. 2019. A reusable battery-free RFID temperature sensor. *IEEE TAP* 67, 10 (2019), 6612–6626.

[49] E Sharp and M Diab. 1960. Van Atta reflector array. *IEEE TAP* 8, 4 (1960), 436–438.

[50] Edoh Shaulov, Samuel Jameson, and Eran Socher. 2017. W-band energy harvesting rectenna array in 65-nm CMOS. In *2017 IEEE MTT-S International Microwave Symposium (IMS)*. 307–310. https://doi.org/10.1109/MWSYM.2017.8059105

[51] Sudhir Shrestha, Jeevan Vemagiri, Mangilal Agarwal, and Kody Varahramyan. 2007. Transmission line reflection and delay-based ID generation scheme for RFID and other applications. *International Journal of Radio Frequency Identification Technology and Applications* 1, 4 (2007), 401–416.

[52] Elahe Soltanaghaei, Akarsh Prabhakara, Artur Balanuta, Matthew Anderson, Jan M Rabaey, Swarun Kumar, and Anthony Rowe. 2021. Millimetro: mmWave retro-reflective tags for accurate, long range localization. In *Proceedings of ACM MobiCom*.

[53] Kunpeng Song, Dejun Feng, Junjie Wang, Qianpeng Xie, and Lei Liu. 2019. Phase Modulation of Retro-Reflected Radar Echo Signal Using a Microstrip Van-Atta Array. *IEEE Access* 7 (2019).

[54] StereoLabs. 2019. Zed Camera. https://www.stereolabs.com/zed/.

[55] Rainer Storn and Kenneth Price. 1997. Differential evolution a simple evolution strategy for fast optimization. *Dr. Dobb's Journal* 22, 4 (1997), 18–24.

[56] Qinghui Tang, Sandeep KS Gupta, and Loren Schwiebert. 2005. BER performance analysis of an on-off keying based minimum energy coding for energy constrained wireless sensor applications. In *Proceedings of IEEE ICC*, Vol. 4. 2734–2738.

[57] Tracking Using TI. 2017. Traffic Monitoring Object Detection and Tracking Reference Design Using Single-Chip mmWave Radar Sensor.

[58] Christopher R Valenta and Gregory D Durgin. 2014. Harvesting wireless power: Survey of energy-harvester conversion efficiency in far-field, wireless power

transfer systems. *IEEE Microwave Magazine* 15, 4 (2014), 108–120.

[59] Purui Wang, Lilei Feng, Guojun Chen, Chenren Xu, Yue Wu, Kenuo Xu, Guobin Shen, Kuntai Du, Gang Huang, and Xuanzhe Liu. 2020. Renovating road signs for infrastructure-to-vehicle networking: a visible light backscatter communication and networking approach. In *Proceedings of ACM MobiCom*.

[60] Yibin Wu, Jian Kuang, and Xiaoji Niu. 2020. Wheel-INS2: Multiple MEMS IMU-based Dead Reckoning System for Wheeled Robots with Evaluation of Different IMU Configurations. *arXiv preprint arXiv:2012.10593* (2020).

[61] Yibin Wu, Xiaoji Niu, and Jian Kuang. 2020. A Comparison of Three Measurement Models for the Wheel-mounted MEMS IMU-based Dead Reckoning System. *arXiv preprint arXiv:2012.10589* (2020).

[62] Kevin Xu, Dana Koshen, Muratkhan Abdirash, and Jun H Choi. 2019. A Retrodirective Microwave Barcode. In *Proceedings of IEEE MTT-S IMS*.

[63] Kin Shing Bobby Yau. 2015. Planar multi-layer passive retrodirective Van Atta array reflectors at X-band. In *Proceedings of IEEE ISAP*. IEEE.

[64] Zhen-wei Zhao, Ming-gao Zhang, and Zhen-sen Wu. 2001. Analytic specific attenuation model for rain for use in prediction methods. *Springer International Journal of Infrared and millimeter waves* 22, 1 (2001), 113–120.